INTERNATIONAL JOURNAL FOR NUMERICAL AND ANALYTICAL METHODS IN GEOMECHANICS
Int. J. Numer. Anal. Meth. Geomech., **23**, 2075–2095 (1999)

VERTICAL VIBRATIONS OF A RIGID DISK EMBEDDED IN A POROELASTIC MEDIUM

X. ZENG AND R. K. N. D. RAJAPAKSE*

Department of Civil and Geological Engineering, University of Manitoba, Winnipeg, Canada R3T 5V6

SUMMARY

This paper considers the steady-state vertical vibrations of a rigid circular disk embedded at a finite depth below the free surface of a poroelastic medium. Biot's elastodynamic theory for porous media is used in the analysis. General solutions for axisymmetric poroelastic fields are obtained by using Hankel integral transforms. Analytical solutions for influence functions corresponding to four types of buried axisymmetric excitations are derived. The embedded disk problem is fomulated in terms of a set of coupled integral equations for unknown traction and pore pressure jumps across the disk. The kernel functions of the integral equations are the influence functions corresponding to buried vertical, radial and pore pressure ring loads. The system of integral equations is solved numerically by discretizing the disk into several concentric annular rings. Selected numerical solutions for displacements, vertical stress and pore pressure due to a buried fully flexible disk (uniform pressure) are also presented. The vertical compliances of a rigid disk are examined for different depths of embedment, poroelastic materials and hydraulic boundary conditions. Solutions for traction and pore pressure jumps are also examined. The present results are useful in the study of dynamic response of embedded foundations and anchors in poroelastic soils. Copyright © 1999 John Wiley & Sons, Ltd.

KEY WORDS: poroelasticity; dynamic soil–structure interaction; vibrations; foundations; anchors; impedance

INTRODUCTION

The classical theory of dynamic poroelasticity developed by Biot[1,2] has been used for more than four decades to study a variety of interesting problems involving saturated elastic porous media. Biot's theory is widely applied in geomechanics to analyse consolidation effects under static and dynamic loading. Among others, Senjuntichai and Rajapakse,[3] Beskos,[4] and Philippacopoulos[5] reviewed literature related to wave propagation in elastic porous media. Majority of the theoretical studies based on Biot's elastodynamic theory focus on the derivation of solutions for basic loading configurations. The development of solutions in dynamic poroelasticity for specific applications in geomechanics has not received wide attention as in the case of elastic soils. For example, analytical or semi-analytical solutions for several dynamic poroelastic soil–structures

*Correspondence to: Professor R. K. N. D. Rajapakse, Department of Civil and Geological Engineering, University of Manitoba, 15 Gillson Street, Winnipeg, Manitoba, Canada R3T 5V6

Contract grant sponsor: Natural Sciences and Engineering Research Council of Canada
Contract grant number: A-6507

CCC 0363–9061/99/152075–21$17.50

Received 8 October 1998
Revised 22 February 1999

interaction problems (e.g. embedded foundations, anchors, piles, etc.) have not been considered in the past. The present study is not focusing on finite-element-based solutions.

The classical problem involving interaction between a vertically loaded rigid disk and an elastic medium has been used in geomechanics to examine deformations and stresses of soil– foundation systems.[6] A review of vast literature on this topic is beyond the scope of this study. Given the fact that almost all soils are two-phase systems (soil grains and water), it is much more realistic to examine rigid disk problems within the framework of Biot's dynamic theory of poroelasticity for applications in geomechanics. In recent years, some progress has been made in this direction. For example, Halpern and Christiano,[7,8] Philippacopulos,[9,10] Kassir and Xu,[11] Kassir *et al.*,[12] Bougacha *et al.*[13,14] and Senjuntichai and Rajapakse[15] examined the dynamics of rigid rectangular, circular and strip foundations on the surface of a poroelastic soil. These studies provided useful insight into the influence of poroelastic behaviour on the compliance of rigid surface foundations.

In this paper, the steady-state vertical vibrations of a rigid circular disk embedded at a finite depth in a poroelastic half-space is considered (Figure 1). The cases of a disk on the surface and deeply buried in a poroelastic medium are the two limiting cases of the generalized problem under consideration in the present study. The solutions to this class of problems are useful in the study of embedded foundations, foundations of offshore structures and anchors. To our knowledge, a theoretical study of dynamics of an embedded rigid inclusion in a poroelastic medium has not been reported in the literature. Analytical solutions for influence functions corresponding to buried axisymmetric ring loads derived with the aid of Hankel integral transforms are used to formulate the problem. A system of fully coupled singular integral equations is established in terms of the jumps in tractions and pore pressure across the disk. The integral equation is solved

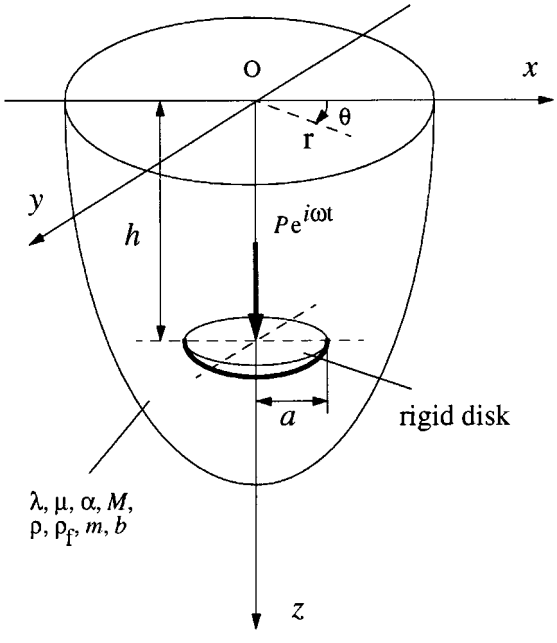

Figure 1. Rigid circular disk embedded in poroelastic medium

numerically by discretizing the disk into concentric annular domains. Selected results for dynamic compliance, and traction and pore pressure jumps are presented to portray the effects of depth of embedment, poroelastic properties and hydraulic boundary conditions on the disk. Solutions for an embedded fully flexible disk (uniform pressure) are also presented. The influence functions corresponding to buried loads derived in the present study are powerful tools that can be used to analyse a variety of other practical problems in geomechanics.

GOVERNING EQUATIONS

Consider the axisymmetric motion of a poroelastic half-space governed by Biot's two-phased linear theory. A cylindrical co-ordinate system $o(r, \theta, z)$ is defined such that the z-axis is perpendicular to the free surface of the half-space, and the motion is axisymmetric with respect to the z-axis (Figure 1). Let u_i and w_i denote the average displacement of the solid matrix and the fluid displacement relative to the solid matrix, in the i-direction ($i = r, z$), respectively. The constitutive relations for a homogeneous poroelastic material can be expressed as[1]

$$\sigma_{rr} = \lambda e + 2\mu \frac{\partial u_r}{\partial r} - \alpha p, \qquad \sigma_{\theta\theta} = \lambda e + 2\mu \frac{u_r}{r} - \alpha p \tag{1a}$$

$$\sigma_{zz} = \lambda e + 2\mu \frac{\partial u_z}{\partial z} - \alpha p, \qquad \sigma_{zr} = \mu \left(\frac{\partial u_r}{\partial z} + \frac{\partial u_z}{\partial r} \right) \tag{1b}$$

$$p = -\alpha M e + M\zeta \tag{1c}$$

where

$$e = \frac{\partial u_r}{\partial r} + \frac{\partial u_z}{\partial z} + \frac{u_r}{r}, \qquad \zeta = -\left(\frac{\partial w_r}{\partial r} + \frac{\partial w_z}{\partial z} + \frac{w_r}{r} \right) \tag{2}$$

and σ_{rr}, $\sigma_{\theta\theta}$, σ_{zz}, and σ_{zr} denote total stress component of the bulk material, e is the dilatation of the solid phase, μ and λ are Lamé's constants of the bulk material, p is the excess pore fluid pressure, ζ is the dilatation of the pore fluid and α, M are Biot's parameters accounting for compressibility of the two-phased material.[1]

The governing equations for axisymmetric motion can be expressed as

$$\begin{aligned}
\mu \nabla^2 u_r + (\lambda + \alpha^2 M + \mu) \frac{\partial e}{\partial r} - \mu \frac{u_r}{r^2} - \alpha M \frac{\partial \zeta}{\partial r} &= \rho \ddot{u}_r + \rho_f \ddot{w}_r \\
\mu \nabla^2 u_z + (\lambda + \alpha^2 M + \mu) \frac{\partial e}{\partial z} - \alpha M \frac{\partial \zeta}{\partial z} &= \rho \ddot{u}_z + \rho_f \ddot{w}_z \\
\alpha M \frac{\partial e}{\partial r} - M \frac{\partial \zeta}{\partial r} &= \rho_f \ddot{u}_r + m \ddot{w}_r + b \dot{w}_r \\
\alpha M \frac{\partial e}{\partial z} - M \frac{\partial \zeta}{\partial z} &= \rho_f \ddot{u}_z + m \ddot{w}_z + b \dot{w}_z
\end{aligned} \tag{3}$$

where an overdot denotes the derivatives of a field variable with respect to the time parameter t, ρ and ρ_f are the mass densities of the bulk material and the pore fluid, respectively, $m = \rho_f/\beta (\beta = \text{porosity})$, is a density-like parameter, b is a parameter accounting for the internal

friction due to the relative motion between the solid matrix and the pore fluid, and defined as the ratio between the fluid viscosity and the intrinsic permeability of the porous medium.

The motion under consideration is assumed to be time-harmonic with a factor of $e^{i\omega t}$, where ω is frequency of the motion and $i = \sqrt{-1}$. The term $e^{i\omega t}$ is henceforth suppressed from all expressions for brevity. It is convenient to non-dimensionalize all length quantities including the co-ordinate frame by selecting the radius of the circular disk as a unit of length. Stresses and pore pressure are non-dimensionalized with respect to the shear modulus μ of the bulk material. All variables are replaced by the non-dimensional quantities, but the previous notations are used for convenience.

The governing partial differential equations are solved by applying a Helmholtz representation for an axisymmetric vector field and a Hankel integral transform with respect to the radial coordinate. The nth-order Hankel integral transform of a function $f(r, z)$ and the inverse transform are defined as[16]

$$\bar{f}(k, z) = \int_0^\infty r f(r, z) J_n(kr)\, dr \tag{4a}$$

$$f(r, z) = \int_0^\infty k \bar{f}(k, z) J_n(kr)\, dk \tag{4b}$$

where J_n and k denote the Bessel function of the first kind of the nth order and the Hankel transform parameter, respectively.

The following general solutions can be obtained for the zeroth-order Hankel transfrom of u_z, w_z, σ_{zz} and p, and the first-order Hankel transform of u_r, w_r and σ_{zr}, respectively.

$$\bar{u}_r = -k(Ae^{\gamma_1 z} + Be^{-\gamma_1 z} + Ce^{\gamma_2 z} + De^{-\gamma_2 z}) - \gamma_3(Ee^{\gamma_3 z} - Fe^{-\gamma_3 z}) \tag{5a}$$

$$\bar{u}_z = \gamma_1(Ae^{\gamma_1 z} - Be^{-\gamma_1 z}) + \gamma_2(Ce^{\gamma_2 z} - De^{-\gamma_2 z}) + k(Ee^{\gamma_3 z} + Fe^{-\gamma_3 z}) \tag{5b}$$

$$\bar{w}_r = -k(\chi_1(Ae^{\gamma_1 z} + Be^{-\gamma_1 z}) + \chi_2(Ce^{\gamma_2 z} + De^{-\gamma_2 z})) - \gamma_3\chi_3(Ee^{\gamma_3 z} - Fe^{-\gamma_3 z}) \tag{5c}$$

$$\bar{w}_z = \gamma_1\chi_1(Ae^{\gamma_1 z} - Be^{-\gamma_1 z}) + \gamma_2\chi_2(Ce^{\gamma_2 z} - De^{-\gamma_2 z}) + k\chi_3(Ee^{\gamma_3 z} + Fe^{-\gamma_3 z}) \tag{5d}$$

$$\bar{\sigma}_{zr} = -2k(\gamma_1(Ae^{\gamma_1 z} - Be^{-\gamma_1 z}) + \gamma_2(Ce^{\gamma_2 z} - De^{-\gamma_2 z})) - S_1(Ee^{\gamma_3 z} + Fe^{-\gamma_3 z}) \tag{5e}$$

$$\bar{\sigma}_{zz} = \beta_1(Ae^{\gamma_1 z} + Be^{-\gamma_1 z}) + \beta_2(Ce^{\gamma_2 z} + De^{-\gamma_2 z}) + 2k\gamma_3(Ee^{\gamma_3 z} - Fe^{-\gamma_3 z}) \tag{5f}$$

$$\bar{p} = \eta_1(Ae^{\gamma_1 z} + Be^{-\gamma_1 z}) + \eta_2(Ce^{\gamma_2 z} + De^{-\gamma_2 z}) \tag{5g}$$

where A, B, C, D, E and F are arbitrary functions to be determined from the boundary and continuity conditions of given problem. The variables γ_i, χ_i, etc., appearing in the above equations are defined in the appendix.

The fluid discharge is defined as the time derivative of the fluid displacement relative to the solid matrix.[17] The fluid discharge non-dimensionalized with respect to $\sqrt{\mu/\rho}$ can be expressed as

$$q_n = i\delta w_n, \quad n = r, z \tag{6}$$

INFLUENCE FUNCTIONS

The formulation presented in an ensuing section for an embedded disk requires the influence functions for axisymmetric ring loads and fluid sources applied in the interior of a poroelastic

half-space. In this section, boundary-value problems related to interior axisymmetric loading (ring/annular/point) are considered. The loads are applied at a depth z' below the free surface of the half-space. Four basic loading configurations are considered. These involve a buried vertical load, a radial shear load, a fluid source and a pore pressure (fluid stress) load. The solutions can be obtained by defining a fictitious plane at $z = z'$ and treating the half-space as a two-domain boundary-value problem.[18] General solutions for each domain are given by equations (5) and (6) together with arbitrary functions A_i to F_i, where a subscript $i (i = 1, 2)$ is used to identify the domain number. For domain 2, set $A_2 = C_2 = E_2 = 0$ to guarantee the regularity of the solutions at infinity.

The boundary conditions corresponding to a fully permeable top surface ($z = 0, 0 \leqslant r < \infty$) can be expressed as

$$\sigma_{zn}^{(1)}(r, 0) = 0, \quad n = r, z \tag{7a}$$

$$p^{(1)}(r, 0) = 0 \tag{7b}$$

where a superscript (1) is used to denote the domain number.

The continuity conditions at the fictitious plane ($z = z', 0 \leqslant r < \infty$) for buried vertical/radial loads applied to solid matrix and a fluid source are given by

$$u_n^{(1)}(r, z') - u_n^{(2)}(r, z') = 0, \quad n = r, z \tag{8a}$$

$$p^{(1)}(r, z') - p^{(2)}(r, z') = 0 \tag{8b}$$

$$\sigma_{zn}^{(1)}(r, z') - \sigma_{zn}^{(2)}(r, z') = \frac{T_n(r)}{\mu}, \quad n = r, z \tag{8c}$$

$$w_z^{(1)}(r, z') - w_z^{(2)}(r, z') = \sqrt{\frac{\rho}{\mu}} \frac{\mathrm{i}Q(r)}{\delta} \tag{8d}$$

where $T_n(r)$ denotes the intensity of the buried load in the n-direction ($n = r, z$), and $Q(r)$ denotes the intensity of the fluid source.

In order to simulate the pore pressure discontinuity across an impermeable disk, it is necessary to consider an internal fluid pressure (stress) loading with no discontinuity in solid skeleton stresses. Such a problem is described by the following conditions in addition to the equation (7):

$$p^{(2)}(r, z') - p^{(1)}(r, z') = \frac{P(r)}{\mu} \tag{9a}$$

$$\sigma_{zz}^{(1)}(r, z') - \sigma_{zz}^{(2)}(r, z') = \alpha \frac{P(r)}{\mu} \tag{9b}$$

$$\sigma_{zr}^{(1)}(r, z') - \sigma_{zr}^{(2)}(r, z') = 0 \tag{9c}$$

$$w_z^{(1)} - w_z^{(2)} = 0 \tag{9d}$$

where $P(r)$ denotes the intensity of fluid pressure discontinuity at the depth $z = z'$.

The required influence functions are obtained by solving the boundary-value problems corresponding to each loading case separately. It is useful to present explicit solutions for non-zero arbitrary coefficients appearing in the general solutions given by equations (5) and (6) since

influence functions corresponding to different types of axisymmetric loads (e.g. point loads, ring loads, annular rings, etc.) can be derived by simply substituting the appropriate Hankel transform of the load. Therefore, the present approach is more versatile in deriving solutions for a variety of buried axisymmetric loads than the approach followed by Phillippacopoulos[5] for point loads in a half-space, which requires the corresponding full-space solutions as the starting point. The present approach does not require the full-space solutions and can be used to derive the full-space solution from the half-space solution through a simple application of limits. The solutions for arbitrary functions corresponding to different types of loads are given below.

Arbitrary functions for vertical loading:

$$A_1 = \frac{\eta_2 e^{-\gamma_1 z'}}{2\mu N_1} \bar{T}_z(k) \tag{10a}$$

$$B_1 = \frac{\eta_2 (v_5 e^{-\gamma_1 z'} + 2k^2 v_3 e^{-\gamma_2 z'} - 4k^2 S_1 v_1 e^{-\gamma_3 z'})}{2\mu N_1 R} \bar{T}_z(k) \tag{10b}$$

$$C_1 = -\frac{\eta_1 e^{-\gamma_2 z'}}{2\mu N_1} \bar{T}_z(k) \tag{10c}$$

$$D_1 = \frac{\eta_1 (2k^2 v_4 e^{-\gamma_1 z'} - v_6 e^{-\gamma_2 z'} + 4k^2 S_1 v_1 e^{-\gamma_3 z'})}{2\mu N_1 R} \bar{T}_z(k) \tag{10d}$$

$$E_1 = \frac{k v_1 e^{-\gamma_3 z'}}{2\mu \gamma_3 N_1} \bar{T}_z(k) \tag{10e}$$

$$F_1 = \frac{k v_2 (v_4 e^{-\gamma_1 z'} - v_3 e^{-\gamma_2 z'}) + k v_1 v_7 e^{-\gamma_3 z'}}{2\mu \gamma_3 N_1 R} \bar{T}_z(k) \tag{10f}$$

$$B_2 = B_1 - A_1 e^{2\gamma_1 z'}, \quad D_2 = D_1 - C_1 e^{2\gamma_2 z'}, \quad F_2 = F_1 + E_1 e^{2\gamma_3 z'} \tag{10g}$$

where

$$v_1 = \eta_1 - \eta_2, \quad v_2 = \eta_1 \beta_2 - \eta_2 \beta_1, \quad v_3 = 4\eta_1 \gamma_2 \gamma_3, \quad v_4 = 4\eta_2 \gamma_3 \gamma_1 \tag{11}$$

$$v_5 = S_1 v_2 - k^2 (v_3 + v_4), \quad v_6 = S_1 v_2 + k^2 (v_3 + v_4), \quad v_7 = S_1 v_2 + k^2 (v_3 - v_4) \tag{12}$$

and

$$N_1 = 2k^2 v_1 - v_2, \quad R = -S_1 v_2 + k^2 (v_3 - v_4) \tag{13}$$

In equation (10), $\bar{T}_z(k)$ is the zeroth-order Hankel transform of the applied axisymmetric vertical load at $z = z'$. In the case of a vertical point load of magnitude P_0,

$$\bar{T}_z(k) = \frac{P_0}{2\pi} \tag{14}$$

For a vertical ring load of radius s and intensity p_0 per unit length,

$$\bar{T}_z(k) = p_0 s J_0(ks) \tag{15}$$

and for a vertical patch load of radius a (unit radius) and uniform intensity p_0,

$$\bar{T}_z(k) = \frac{p_0 J_1(k)}{k} \tag{16}$$

The solutions corresponding to vertical loading applied to a poroelastic full space can be derived by setting $B_1 = D_1 = F_1 = 0$ and $|z - z'| = |z|$, where the centre of the load is now defined as the origin of the cylindrical co-ordinate system. The same procedure can be used in the ensuing sections to obtain full-space solutions for radial, fluid source and fluid pressure loading.

Arbitrary functions for radial loading:

$$A_1 = \frac{k\eta_2 \mathrm{e}^{-\gamma_1 z'}}{2\mu\gamma_1 N_2}\,\bar{T}_r(k) \tag{17a}$$

$$B_1 = \frac{k(\eta_2 v_5 \mathrm{e}^{-\gamma_1 z'} + 2k^2\eta_1 v_4 \mathrm{e}^{-\gamma_2 z'} - S_1 v_1 v_4 \mathrm{e}^{-\gamma_3 z'})}{2\mu\gamma_1 N_2 R}\,\bar{T}_r(k) \tag{17b}$$

$$C_1 = -\frac{k\eta_1 \mathrm{e}^{-\gamma_2 z'}}{2\mu\gamma_2 N_2}\,\bar{T}_r(k) \tag{17c}$$

$$D_1 = \frac{k(2k^2\eta_2 v_3 \mathrm{e}^{-\gamma_1 z'} - \eta_1 v_6 \mathrm{e}^{-\gamma_2 z'} + S_1 v_1 v_3 \mathrm{e}^{-\gamma_3 z'})}{2\mu\gamma_2 N_2 R}\,\bar{T}_r(k) \tag{17d}$$

$$E_1 = \frac{v_1 \mathrm{e}^{-\gamma_3 z'}}{2\mu N_2}\,\bar{T}_r(k) \tag{17e}$$

$$F_1 = \frac{4k^2 v_2(\eta_2 \mathrm{e}^{-\gamma_1 z'} - \eta_1 \mathrm{e}^{-\gamma_2 z'}) + v_1 v_7 \mathrm{e}^{-\gamma_3 z'}}{2\mu N_2 R}\,\bar{T}_r(k) \tag{17f}$$

$$B_2 = B_1 + A_1 \mathrm{e}^{2\gamma_1 z'}, \quad D_2 = D_1 + C_1 \mathrm{e}^{2\gamma_2 z'}, \quad F_2 = F_1 - E_1 \mathrm{e}^{2\gamma_3 z'} \tag{17g}$$

where

$$N_2 = v_1(k^2 - \gamma_3^2) \tag{18}$$

and $\bar{T}_r(k)$ is the first-order Hankel transform of the applied radial loading. In the case of an axisymmetric radial ring load of radius s and intensity p_0 per unit length,

$$\bar{T}_r(k) = p_o s J_1(ks) \tag{19}$$

Arbitrary functions for fluid source:

$$A_1 = \frac{\mathrm{e}^{-\gamma_1 z'}}{2\delta(\chi_1 - \chi_2)\gamma_1}\,\mathrm{i}\sqrt{\frac{\rho}{\mu}}\,\bar{Q}(k) \tag{20a}$$

$$B_1 = \frac{v_5 \mathrm{e}^{-\gamma_1 z'} + 2k^2 v_4 \mathrm{e}^{-\gamma_2 z'}}{2\delta(\chi_1 - \chi_2)\gamma_1 R}\,\mathrm{i}\sqrt{\frac{\rho}{\mu}}\,\bar{Q}(k) \tag{20b}$$

$$C_1 = \frac{e^{-\gamma_2 z'}}{2\delta(\chi_2 - \chi_1)\gamma_2} i \sqrt{\frac{\rho}{\mu}} \bar{Q}(k) \tag{20c}$$

$$D_1 = \frac{2k^2 v_3 e^{-\gamma_1 z'} - v_6 e^{-\gamma_2 z'}}{2\delta(\chi_1 - \chi_2)\gamma_2 R} i \sqrt{\frac{\rho}{\mu}} \bar{Q}(k) \tag{20d}$$

$$E_1 = 0 \tag{20e}$$

$$F_1 = -\frac{2kv_2(e^{-\gamma_1 z'} - e^{-\gamma_2 z'})}{\delta(\chi_2 - \chi_1)R} i \sqrt{\frac{\rho}{\mu}} \bar{Q}(k) \tag{20f}$$

$$B_2 = B_1 + A_1 e^{2\gamma_1 z'}, \quad D_2 = D_1 + C_1 e^{2\gamma_2 z'}, \quad F_2 = F_1 \tag{20g}$$

where $\bar{Q}(k)$ is the zeroth-order Hankel transform of the applied fluid source.

In the case of a point fluid source of strength Q_0 at the point $(0, z')$,

$$\bar{Q}(k) = \frac{Q_0}{2\pi} \tag{21}$$

For a ring fluid source of radius s and intensity q_0 per unit length,

$$\bar{Q}(k) = q_0 s J_0(ks) \tag{22}$$

and for a fluid source of uniform intensity q_0 over a circular patch of radius a (unit radius),

$$\bar{Q}(k) = \frac{q_0 J_1(k)}{k} \tag{23}$$

From equations (20), it is evident that the wave fields in a full space due to an applied fluid source do not create a rotational wave since $E_1 = 0$.

Arbitrary functions for applied fluid pressure:

$$A_1 = \frac{-(\lambda^* + 2) L_2^2 e^{-\gamma_1 z'}}{2\mu N_1} \bar{P}(k) \tag{24a}$$

$$B_1 = \frac{-(\lambda^* + 2)[v_5 L_2^2 e^{-\gamma_1 z'} + 2k^2 \eta_2 (\beta_3 e^{-\gamma_2 z'} - \beta_5 e^{-\gamma_3 z'})]}{2\mu N_1 R} \bar{P}(k) \tag{24b}$$

$$C_1 = \frac{(\lambda^* + 2) L_1^2 e^{-\gamma_2 z'}}{2\mu N_1} \bar{P}(k) \tag{24c}$$

$$D_1 = \frac{(\lambda^* + 2)[v_6 L_1^2 e^{-\gamma_1 z'} - 2k^2 \eta_1 (\beta_4 e^{-\gamma_2 z'} + \beta_5 e^{-\gamma_3 z'})]}{2\mu N_1 R} \bar{P}(k) \tag{24d}$$

$$E_1 = -\frac{k(\lambda^* + 2)(L_1^2 - L_2^2) e^{-\gamma_3 z'}}{2\mu\gamma_3 N_1} \bar{P}(k) \tag{24e}$$

$$F_1 = -\frac{k(\lambda^* + 2)[v_2(\beta_4 e^{-\gamma_1 z'} - \beta_3 e^{-\gamma_2 z'}) + v_7(L_1^2 - L_2^2) e^{-\gamma_3 z'}]}{2\mu\gamma_3 N_1 R} \bar{P}(k) \tag{24f}$$

$$B_2 = B_1 - A_1 e^{2\gamma_1 z'}, \quad D_2 = D_1 - C_1 e^{2\gamma_2 z'}, \quad F_2 = F_1 + E_1 e^{2\gamma_3 z'} \tag{24g}$$

where

$$\beta_3 = 4\gamma_2\gamma_3 L_1^2, \quad \beta_4 = 4\gamma_3\gamma_1 L_2^2, \quad \beta_5 = 2S_1(L_1^2 - L_2^2) \tag{25}$$

and $\bar{P}(k)$ is the Hankel integral transform of the zeroth order of the applied fluid pressure.

In the case of a fluid pressure discontinuity of intensity p_0 over a circular ring of radius s,

$$\bar{P}(k) = p_0 s J_0(ks) \tag{26a}$$

and for a uniform pore pressure discontinuity of p_0 over a circular area of unit radius

$$\bar{P}(k) = p_0 J_1(k)/k \tag{26b}$$

VERTICAL VIBRATIONS OF AN EMBEDDED RIGID DISK

Consider the steady-state vertical excitation of a rigid, massless disk of radius a (zero thickness), embedded at a depth h in a poroelastic half-space, as shown in Figure 1. The disk is assumed to undergo time-harmonic vertical displacement $\Delta_z e^{i\omega t}$, where Δ_z is the amplitude of the motion.

In the formulation, the buried disk is replaced by traction and pore pressure jumps of unknown intensities applied over a circular area of radius a at a depth h below the free surface of an identical poroelastic half-space. The relationship between unknown tractions and pore pressure jumps on S ($0 \leqslant r \leqslant a$, $z = h$) and the generalized displacements of S can be expressed in terms of the following integral equation:

$$\int_0^a G_{ij}(r, h; r', h)\, T_j(r', h)\, \mathrm{d}r' = \Delta_i, \quad i = r, z, p \tag{27}$$

where summation is implied over the index $j = r, z, p$.

In equation (27), T_r, T_z denote jumps in tractions in the radial and vertical direction, respectively, T_p is the jump in pore pressure over the contact surface S if the disk is impermeable (for a fully permeable disk $T_p \equiv 0$); Δ_z and Δ_r ($\equiv 0$) are the vertical and radial displacements at a point on S, Δ_p is the relative fluid displacement normal to S ($\Delta_p = 0$ for an impermeable disk), $G_{ij}(r, h; r', h)$ denote the radial displacement ($i = r$), vertical displacement ($i = z$) and relative fluid displacement normal to S ($i = p$) at a point (r, h) on S due to radial ($j = r$), vertical ($j = z$) and fluid pressure ($j = p$) ring loads through the point (r', h) on S. It should be noted that for a fully permeable disk $i, j = r, z$ in equation (27) since there is no jump in pore pressure across S. Furthermore, for a fully permeable disk under smooth contact $i, j = z$ only in equation (27).

The solutions for influence function G_{ij} are directly obtained from the preceding section. Equation (27) represents three fully coupled system of singular integral equations with a complex kernel G_{ij} expressed in terms of semi-infinite integrals. A formal analytical solution to this type of a coupled singular integral equation system has not been considered previously. Luco and Westmann[19] considered a set of coupled singular integral equations similar to equation (27) for the case of a rigid strip footing on an ideal elastic half-space. They obtained a complete solution of the integral equation system for the incompressible case and a first approximation valid at low frequencies for arbitrary Poisson's ratio. The final integral equation system was numerically solved.[19] The classical problem involving smooth contact between an elastic medium and a rigid circular disk has also been formulated in terms of Fredholm integral equations in literature (References 20, 12 and others). For dynamic problems, the resulting integral equation has to be

solved numerically for all cases. This well established approach can also be used in the present case for smooth contact ($T_r = 0$) of a fully permeable ($T_p = 0$) buried disk. However, such an approach is not used here since the intention is to solve the disk problem under full mechanical and hydraulic contact conditions for an arbitrary set of material properties.

In the present study, the fully coupled equation system for an impermeable disk is solved by discretizing the contact surface S into N annular rings[21] of thickness Δr_j. It is assumed that T_z and T_p within each ring are constant and T_r varies proportionally with the radius. A discrete version of equation (27) can be expressed as

$$\Delta_i(r_k, h) = \sum_{l=1}^{N} \bar{G}_{ij}(r_k, h; r_l, h)\, T_j(r_l, h), \quad i, j = r, z, p \tag{28}$$

where $\bar{G}_{ij}(r_k, h; r_l, h)$ denotes the displacement in the i-direction at the kth node due to a generalized ring load of unit intensity applied in the j-direction over an annular ring corresponding to the lth node with coordinates (r_l, h), and

$$\bar{G}_{ij} = \int_{r_{l-1/2}}^{r_{l+1/2}} G_{ij}\, \mathrm{d}s \tag{29}$$

where $r_{l-1/2}$ and $r_{l+1/2}$ denote the inner and outer radii of the tributary area corresponding to the lth node.

Note that the integration with respect to s (radial direction) in equation (29) can be carried out analytically that result in an explicit solution for $\bar{G}_{ij}$ in terms of semi-infinite integrals. It can be also shown that the resulting $\bar{G}_{ij}(r_k, h; r_l, h)$ corresponding to loading over an annular region is non-singular.

The above linear simultaneous equation system, is solved for $T_{ik} = T_i(r_k, h)$, where $k = 1, 2, \ldots, N$, by setting $\Delta_z(r_k, h) = 1$, $\Delta_r(r_k, h) = 0$ and $\Delta_p(r_k, h) = 0$ for an impermeable rigid disk.

The total vertical load P is given by the following integral of the total vertical contact traction jump over the surface S (including both T_z acting on the solid matrix and the pore pressure jump T_p).

$$\begin{aligned} P &= \int_0^a 2\pi r(T_z + \alpha T_p)\, \mathrm{d}r \\ &= \sum_{k=1}^{N} \pi(r_{k+1/2}^2 - r_{k-1/2}^2)(T_{zk} + \alpha T_{pk}) \end{aligned} \tag{30}$$

NUMERICAL RESULTS AND DISCUSSION

The major computational effort required in the solution of the embedded disk problem involves the computation of $\bar{G}_{ij}$ in equation (28). The solutions for $\bar{G}_{ij}$ appear in terms of semi-infinite integrals with a complex-valued integrand. These integrals cannot be evaluated analytically. Analytical evaluation of $\bar{G}_{ij}$ is not possible even for the special case of ideal elastic materials. In view of the complexity of the integrands, it is natural to adopt a suitable numerical quadrature scheme. By treating k as a complex variable, the singularities of the integrands can be examined. The important singularities of the integrand are the branch points defined by γ_i (see the appendix) and poles of the function R defined by equation (13). The branch points are given by L_1, L_2 and

S defined in the appendix. It is noted that L_1, L_2 and S are the wave numbers corresponding to the three kinds of dispersive and dissipative body waves propagating in a poroelastic solid identified by Biot[2] as the dilatational wave of the first king (L_1), dilatational wave of the second kind (L_2) and a rotational were (S). The factor R in the denominator of the integrand of integrals of $\bar{G}_{ij}$ [equations (10), (17), (20) and (24)] is the Rayleigh equation corresponding to a poroelastic half-space governing the surface waves. The locations of Rayleigh poles are given by

$$R = -S_1 v_2 + k^2(v_3 - v_4) = 0 \tag{31}$$

In reality, all materials have some internal friction (i.e. $b \neq 0$) and the Rayleigh wave in a poroelastic half-space is also dispersive and dissipative like body waves. The presence of material attenuation results in branch points and poles of the integrands which are complex-valued quantities with negative imaginary parts. Therefore, the real k-axis is free from any singularities and $\bar{G}_{ij}$ can be evaluated by direct numerical integration along the real k-axis. For the limiting case ($b = 0$), the integration can be carried along a distorted contour in the first quadrant of the complex plane.[3,22]

For the numerical evaluation of $\bar{G}_{ij}$, the authors used a globally adaptive numerical quadrature scheme.[23] The scheme subdivides the interval of integral and uses a 21-point Gauss–Kronrod rule to estimate the integral over each subinterval. The error for each subinterval is estimated by comparison of the result obtained by 21-point Gauss–Kronrod rule with that by 10-point Gauss quadrature rule. The subinterval with the largest estimated error is then bisected and this procedure is applied to both halves. This bisection procedure is continued until the error criterion is reached. The accuracy of the numerical integration scheme is checked by comparing with the solutions in Reference 22 for a time-harmonic uniform vertical patch load in the interior of an ideal elastic half-space. Excellent agreement with Reference 22 is noted confirming the high accuracy of the numerical integration scheme. Additional comparisons are done in an ensuing section. The case of an ideal elastic medium is simulated by setting the relevant poroelastic material properties to negligibly small values.

To demonstrate the essential features of the influence function $\bar{G}_{ij}$, the response of a few poroelastic half-spaces of different materials is considered. An ideal elastic material and three poroelastic materials identified as material A, B, and C are considered in the numerical study. The non-dimensional parameter λ^*, is equal to 1·0 for the ideal elastic material. The properties of the three poroelastic materials are: $\lambda^* = 1{\cdot}0$, $M^* = 12{\cdot}2$, $\rho^* = 0{\cdot}53$, $m^* = 1{\cdot}1$ and $\alpha = 0{\cdot}97$. In addition $b = 0{\cdot}001$, 2·3, and 10·0 for materials A, B, and C, respectively. The response due to a uniform vertical loading of intensity f_0 over a circular patch of radius a (unit radius) at a depth a below the free surface of a half-space is computed. This case represents a fully flexible circular footing/anchor buried in a poroelastic soil. The locations of branch points and poles of the integrands of influence functions corresponding to the ideal elastic material and the three poroelastic materials are given in Table I. As shown in Table I, the branch points and poles of the integrands are complex-valued, and the real k-axis is free from any singularity.

Figures 2 and 3 show nondimensional vertical displacement, $u^*_{zz}(= \mu u_z / f_0 a)$ of the free surface and along the z-axis. A non-dimensional frequency δ (defined by equation (34) in the appendix) is used in the numerical study. The vertical deflections depend significantly on the frequency of excitation. Both the real and the imaginary parts of surface displacements become more oscillatory as the frequency of excitation increases. Oscillations in the displacement profile along the z-axis is comparatively smaller with increasing frequency. The vertical displacement along the

Table I. Branch points and poles corresponding to different materials

Material	δ	Branch points			Pole
		k_{L1}	k_{L2}	k_S	k_R
Elastic	0·5		(0·28868, 0·00000)	(0·50000, 0·00000)	(0·54383, 0·00000)
A	0·5	(0·30180, −0·00032)	(0·12392, −0·00002)	(0·43146, −0·00013)	(0·47035, −0·00015)
B	0·5	(0·52561, −0·43249)	(0·13122, −0·00115)	(0·49675, −0·01454)	(0·53415, −0·02187)
C	0·5	(1·01713, −0·97231)	(0·13139, −0·00027)	(0·49982, −0·00350)	(0·53144, −0·00826)
Elastic	2·0		(1·15470, 0·00000)	(2·00000, 0·00000)	(2·17533, 0·00000)
A	2·0	(1·20720, −0·00032)	(0·49569, −0·00002)	(1·72585, −0·00013)	(1·88139, −0·00015)
B	2·0	(1·36799, −0·65995)	(0·51707, −0·01368)	(1·87893, −0·13577)	(2·04224, −0·16076)
C	2·0	(2·17518, −1·81768)	(0·52500, −0·00426)	(1·98891, −0·05389)	(2·13696, −0·08285)

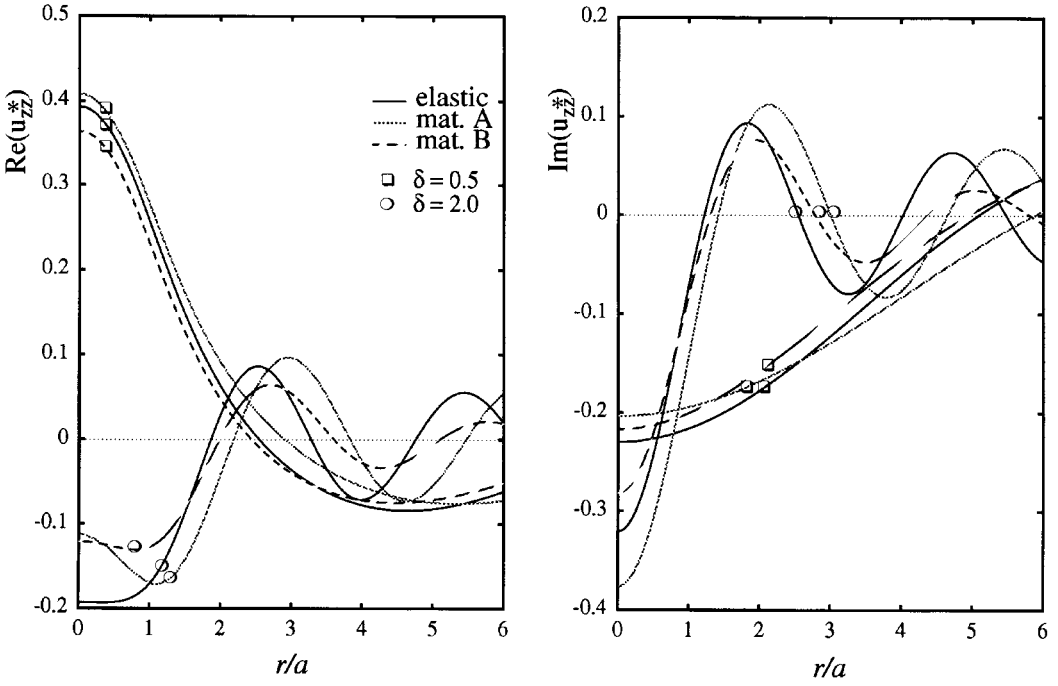

Figure 2. Vertical displacements along the free surface due to buried uniform vertical patch load

surface is substantially different for the three material at higher frequencies. However, at low frequencies ($\delta = 0{\cdot}5$), the response shows little dependence on the material properties. In the case of material B, vertical displacements show rapid decay with the radial distance when compared to the other two materials at $\delta = 2{\cdot}0$. The differences in the deflection profiles are more dominant on or near the free surface. The real part of the vertical deflections show a kink at the level of loading. However, the imaginary part is smooth at this level. The deflections for all three materials decay rapidly with depth reaching negligible values for $z/a > 6{\cdot}0$.

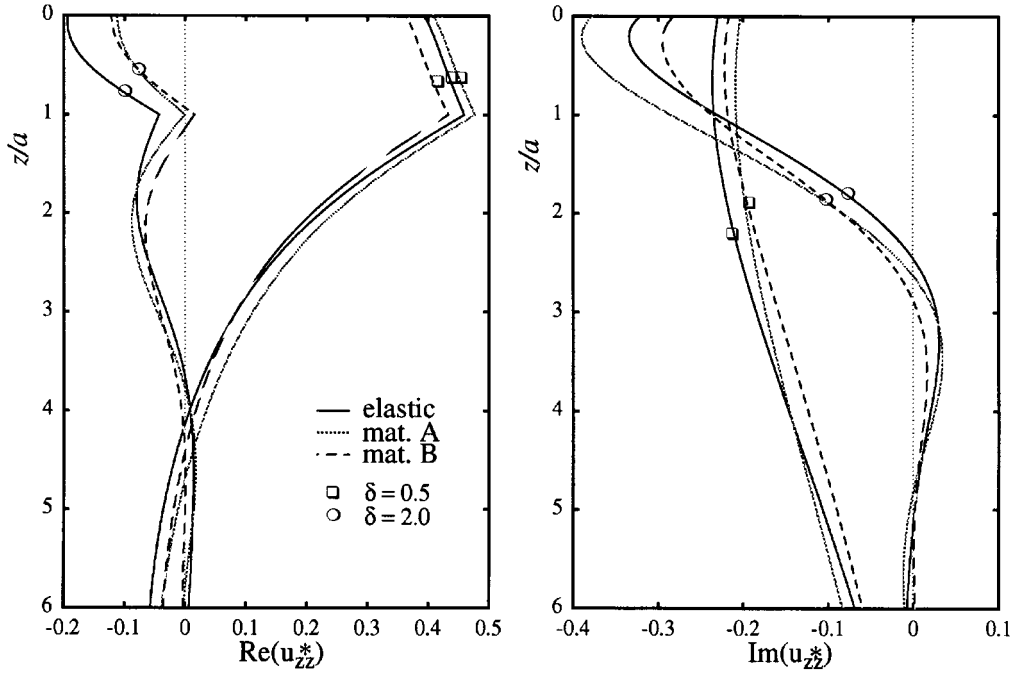

Figure 3. Vertical displacements along the z-axis due to buried uniform vertical patch load

Figures 4 and 5 show the non-dimensional vertical total stress, $\sigma^*_{zzz}(= \sigma_{zz}/f_0)$ and non-dimensional pore pressure $p^*_z(= p/f_0)$ along the z-axis. A unit discontinuity exists in the real part of vertical stress at $z = a$ due to the applied patch load. However the imaginary part of the vertical stress varies smoothly at this level. The real part of the vertical stress varies gradually while the imaginary part shows more oscillations with depth for increasing frequency. The influence of different material parameters on the vertical stress is almost negligible at $\delta = 0{\cdot}5$, but become significant with increasing frequency. The vertical stress is negligible for $z/a > 5{\cdot}0$. The non-dimensional pore pressure depends significantly on the frequency of excitation and the poroelastic materials properties when compared to the vertical stress. As expected, the magnitude of pore pressure is generally smaller than the vertical stress and decays quite rapidly with depth. It shows more oscillations with depth especially near the loading level. Since the applied vertical load is completely taken by the solid skeleton, there is no discontinuity in the pore pressure profile at $z = a$. The magnitude of pore pressure appears to be higher in the case of material C. Since only b^* is different for the three poroelastic materials, it can be argued that an increase in relative friction between fluid and solid phases contributes to increasing pore pressures. Given that b^* is related to permeability inversely, it also means that as permeability decreases more pore pressure is generated in the medium.

Vertical compliance of buried disks

The relationship between the magnitude of vertical load P and the magnitude of vertical displacement Δ_z of a buried disk can be obtained from the numerical solution of equations (28)

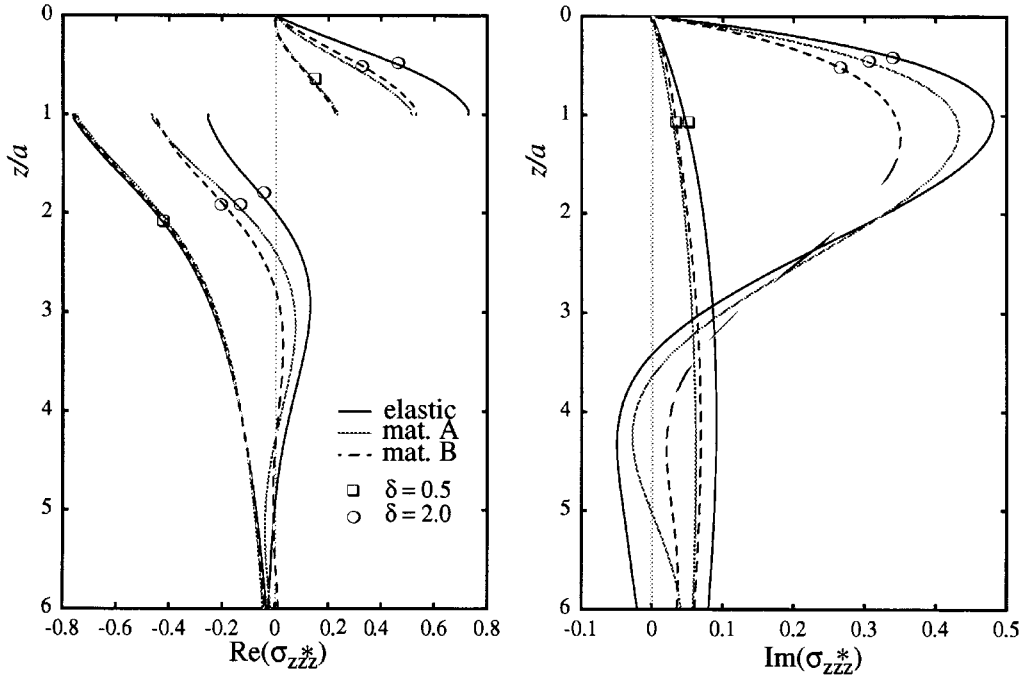

Figure 4. Vertical stresses along the z-axis due to buried uniform vertical patch load

and (30). The vertical compliance of an embedded disk is defined as

$$C_{vv} = \frac{\Delta_z}{P} \tag{32}$$

Dynamic compliances computed in the present study are in the dimensionless form $C^*_{vv} = C_{vv}/C^0_{vv}$, where C^0_{vv} is the vertical compliance of a rigid circular disk on an ideal elastic half-space under static loading ($\delta = 0{\cdot}0$). It can be shown that[6]

$$C^0_{vv} = \frac{1 - v}{4\mu a} \tag{33}$$

where μ and v denote shear modulus and Poisson's ratio of the half-space.

Figure 6 shows a comparison of vertical compliance of a rigid disk in smooth contact with the surface of an ideal elastic half-space (Poisson's ratio = 0·25). Solutions corresponding to the present analysis are based on the reduction of a poroelastic material to an ideal elastic case by setting M^*, ρ^*, m^*, b^*, and α to very small values. For smooth contact problem, equation (28) is solved with $i, j = z$ only. Excellent agreement is noted with solutions reported by Luco and Westmann.[20] The contact surface was discretized by sixteen annular rings of equal thickness in the radial direction. A convergence study was also carried out and the optimum value for N was found to be 16. All subsequent numerical solutions correspond to $N = 16$. Figure 6 also

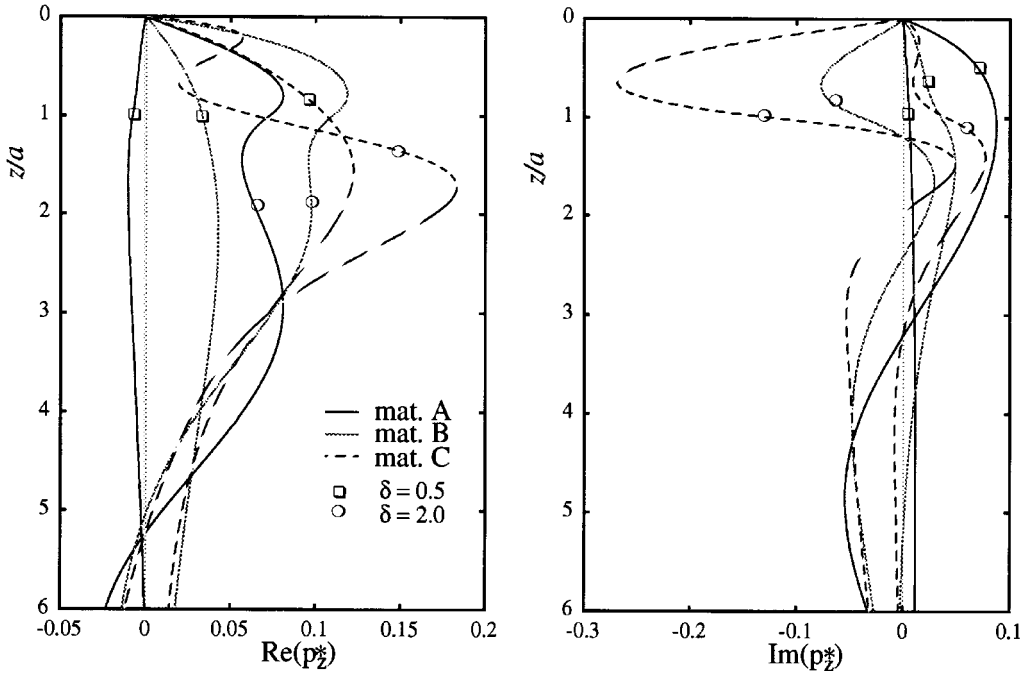

Figure 5. Pore pressure along the z-axis due to buried uniform vertical patch load

shows the vertical compliance of a rigid disk embedded in an ideal elastic half-space when $h/a = 2$. Close agreement with the solutions reported by Pak and Gobert[24] for a rigid disk in smooth contact with the embedding elastic medium is observed. Pack and Gobert solved the embedded disk problem using approximate boundary conditions and the classical reduction[16,20] to a Fredholm integral equation of the second kind. These comparisons confirm the accuracy of the influence functions, formulation of the disk problem and the numerical implementation.

The dynamic response of a rigid disk embedded in a poroelastic half-space is considered in the remainder of this paper. Figure 7 shows the dimensionless vertical compliance of impermeable and fully permeable rigid disks with different depth ratios ($h/a = 0$, 1, 2, 5, 20). The properties of the poroelastic material are those of material B defined previously (i.e. $\lambda^* = 1{\cdot}0$, $M^* = 12{\cdot}2$, $\rho^* = 0{\cdot}53$, $m^* = 1{\cdot}1$, $b^* = 2{\cdot}3$, $\alpha = 0{\cdot}97$). The variation of compliance with non-dimensional frequency δ is smooth for both surface ($h/a = 0{\cdot}0$) and deeply buried ($h/a = 20{\cdot}0$) disks. However for intermediate depths, both the real and imaginary parts of the compliance show oscillations with the frequency. This is a consequence of the standing waves generated between the free surface and the embedded disk that practically vanish for very deep embedments. Similar behaviour is also noted in the Pak and Gobert solutions[24] for the ideal elastic case. The vertical compliance depends significantly on h/a for $0{\cdot}0 < h/a < 5{\cdot}0$. Another feature of the solutions in Figure 7 is the increasing difference between compliances of impervious and pervious disks at high frequencies ($\delta > 2{\cdot}0$). More dissipation of energy is also noted in the case of impervious disks (note that the applied load is resisted both by discontinuities in vertical and radial shearing stresses and by

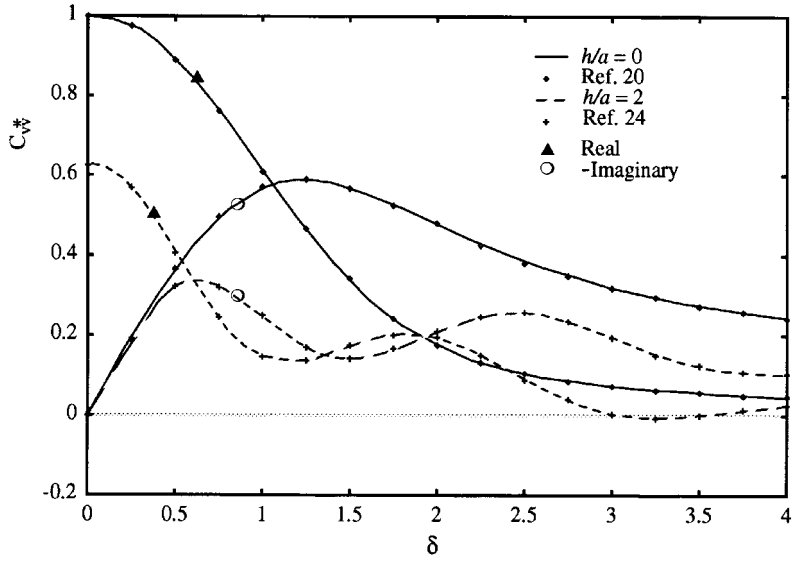

Figure 6. Comparison of vertical compliances of rigid circular disk in an ideal elastic medium

discontinuities in pore pressure) when compared to fully pervious disks. Comparison of solutions neglecting contact radial shear stresses [$T_r = 0$ in equation (28)] showed only minor differences in the frequency range $0 < \delta < 4{\cdot}0$.

Figure 8 shows a comparison of the vertical compliance of an impervious disk embedded in an ideal elastic material ($\lambda^* = 1{\cdot}0$, $\nu = 0{\cdot}25$) and three different poroelastic materials (i.e. materials *B–D*). Materials *B* and *C* are defined previously. The poroelastic properties of material *D* are identical to material *B* except that $b^* = 30{\cdot}0$. Thus material *D* has the highest internal friction due to relative motion between solid and fluid phases. Since b^* is inversely proportional to permeability, it also means that material *B* is the most permeable and material *D* is the least permeable among the three poroelastic materials considered in Figure 8. The solutions correspond to surface ($h = 0$) and embedded ($h = 2a$) disks. At low frequencies ($\delta < 1{\cdot}0$), the influence of material properties on vertical compliance of a buried disk is almost negligible with elastic and poroelastic media showing nearly identical compliances. This trend is changed with increasing frequencies and more significant dependence on the material type is observed. Note that λ^* is identical for all four materials. Once again, the main difference between the three poroelastic materials is the value of b^* and the differences observed in Figure 8 can be interpreted as the dependence on b^*. For surface and embedded disks, the magnitude of the imaginary part of the compliance decreases with increasing b^* for $\delta > 1{\cdot}0$ implying the more dissipative (and less permeable) nature of the material. The real part of vertical compliance of buried disks also decreases with increasing b^* for $1{\cdot}0 < \delta < 3{\cdot}0$ whereas for surface disks the real part of compliance shows more dependence on the material type over the entire frequency range considered. The results shown in Figures 7 and 8 clearly indicate that the ideal elastic solutions cannot be used to approximate the response of buried disks in poroelastic media except at very low frequencies. The general trend of poroelastic effects on the vertical compliance observed in the present study agrees with the observations of Halpern and Christiano[8] for rigid rectangular surface foundations. However, our

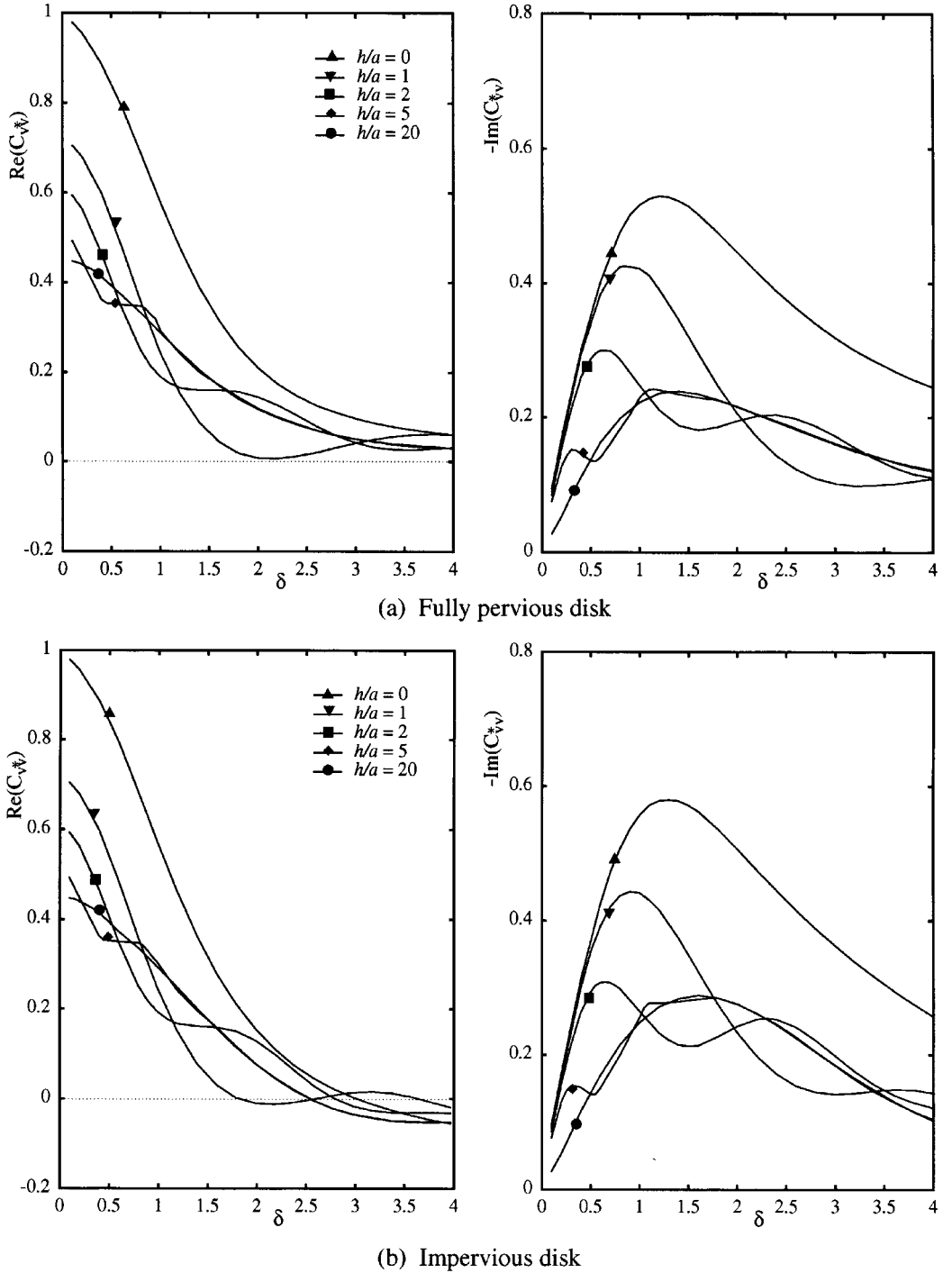

Figure 7. Vertical compliance of rigid disks for different depth of embedment (Material B)

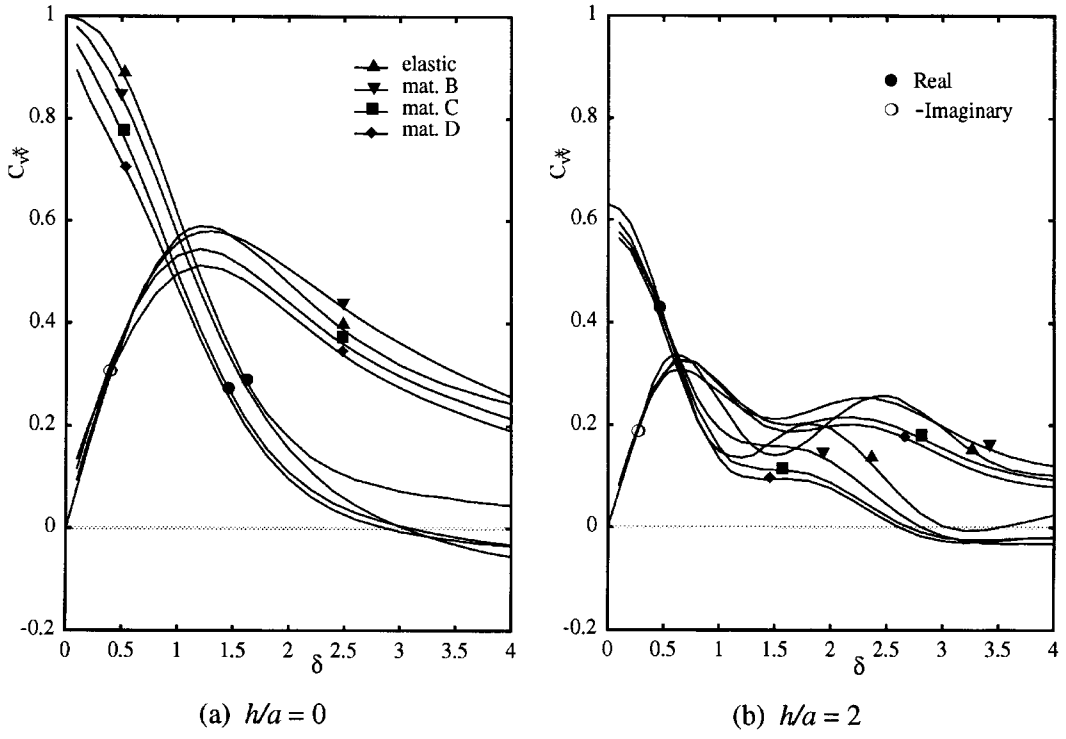

Figure 8. Vertical compliance of rigid disks in different poroelastic media

solutions for vertical compliances are in disagreement with the results of Kassir *et al.*[12] for vertical vibrations of rigid circular disks on the surface. Their results show substantially different magnitudes and trends with frequency, with those for ideal elastic solutions, that appear to be very unrealistic and questionable.

It is useful to examine the distribution of contact tractions T_i under a rigid disk to gain some insight into the load transfer mechanism. Figure 9 shows $T_z\pi a^2/P$ and $T_p\pi a^2/P$ corresponding to an embedded disk ($h/a = 2$) at $\delta = 0{\cdot}5, 2{\cdot}0$. An ideal elastic material ($\lambda^* = 1{\cdot}0$, $\nu = 0{\cdot}25$) and the poroelastic material *B* are considered. The results are shown for impermeable disks in the case of material *B*. The real part of T_z is nearly independent of the frequency and the type of material. The imaginary part shows considerable dependence on frequency and material type with increasing frequency. Both real and imaginary parts of T_z are singular near the edge of the disk. The real part of T_p is negligible but the imaginary part is comparatively larger at $\delta = 2{\cdot}0$. This implies larger amplitudes of T_p and substantial phase differences with T_z at higher frequencies. Both real and imaginary parts of T_p approach zero near the edge of the disk. This implies that the pore pressure jump is not singular at the edge. Based on these results, it can be concluded that negligible pore pressure is generated under an impermeable disk at low frequencies for low values of b^* and that the load is mainly transferred through the solid skeleton. However, at higher frequencies, the load is transferred to the medium through both solid and fluid phases.

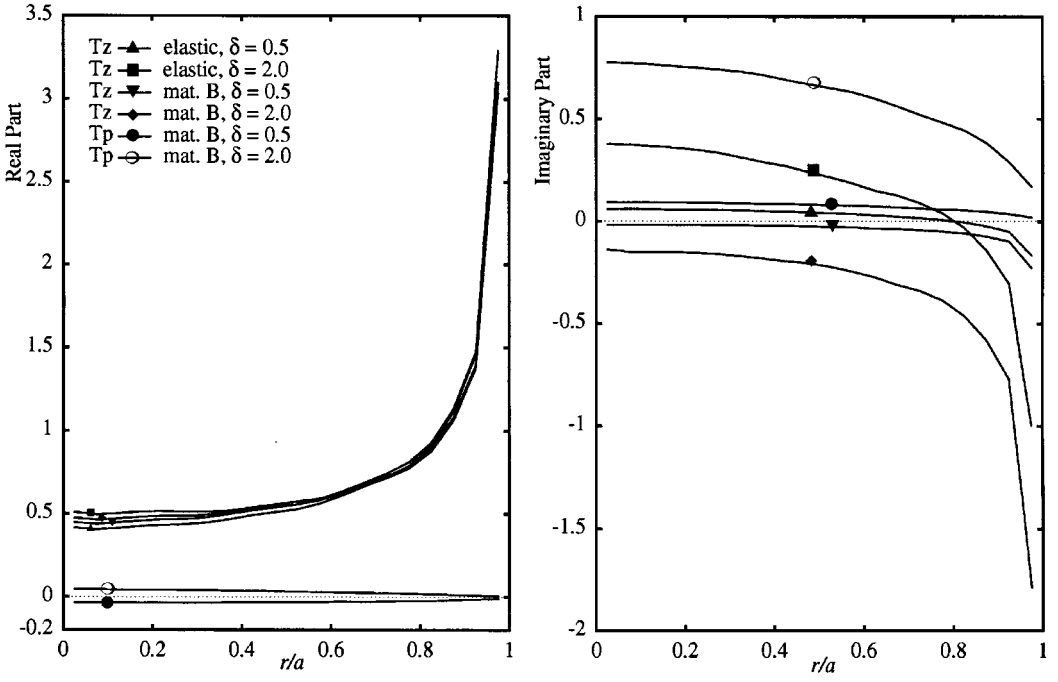

Figure 9. Profiles of vertical stress and pore pressure jumps under rigid disks ($h/a = 2$)

CONCLUSIONS

A complete set of influence functions for displacements, stresses, pore pressure and fluid discharge of a poroelastic half-space subjected to time-harmonic, axisymmetric buried excitations are presented. Analytical solutions for poroelastic fields appear in terms of semi-infinite integrals with complex-valued integrands and Bessel functions. The numerical quadrature scheme employed in the study to compute the influence functions result in stable and accurate solutions. The problem of a fully bonded impermeable disk can be formulated in terms of a set of coupled integral equations. The kernel functions of the integral equations are the influence functions corresponding to buried vertical, radial and fluid pressure excitations. The complexity of the kernel functions eliminate any possible analytical solution of the integral equations. The integral equation can be solved accurately by discretizing the disk into annular rings and evaluating the influence functions numerically by using a globally adaptive quadrature scheme. Numerical solutions for vertical compliance show a considerable dependence on the depth of embedment and the frequency of excitation. In addition, the poroelastic material properties and the hydraulic boundary condition of the disk influence the compliances at high frequencies. An increase in stiffness and radiation damping is noted due to poroelastic effects. Load transfer takes place mainly through the solid skeleton at lower frequencies and through both phases at higher frequencies. The solutions presented in this study are useful in estimating the response and load transfer characteristics of buried foundations and anchors in poroelastic soils. The influence functions presented in this study can be used in boundary element analysis and modelling of other geomechanics problems involving poroelastic media.

ACKNOWLEDGEMENTS

The work presented in this paper was supported by grant A-6507 awarded by the Natural Sciences and Engineering Research Council of Canada.

APPENDIX

For convenience, the material properties: λ, M, ρ_f, m, b and frequency ω are nodimensionalized as

$$\lambda^* = \frac{\lambda}{\mu}, \quad M^* = \frac{M}{\mu}, \quad \rho^* = \frac{\rho_f}{\rho}, \quad m^* = \frac{m}{\rho}, \quad b^* = \frac{ab}{\sqrt{\rho\mu}}, \quad \text{and } \delta = \sqrt{\frac{\rho}{\mu}}\,\omega a \tag{34}$$

The variables γ_i, χ_i, β_i, η_i and S_1 in the general solutions (equation (5)) are defined as

$$\gamma_i = \sqrt{k^2 - L_i^2}, \quad i = 1,\ 2 \tag{35}$$

$$\gamma_3 = \sqrt{k^2 - S^2} \tag{36}$$

$$\chi_i = \frac{(\lambda^* + \alpha^2 M^* + 2)L_i^2 - \delta^2}{\rho^*\delta^2 - \alpha M^* L_i^2}, \quad i = 2 \tag{37}$$

$$\chi_3 = \frac{\rho^*\delta}{\mathrm{i}b^* - m^*\delta} \tag{38}$$

$$\eta_i = (\alpha + \chi_i)M^* L_i^2, \quad i = 1, 2 \tag{39}$$

$$\beta_i = 2\gamma_i^2 - \lambda^* L_i^2 - \alpha\eta_i, \quad i = 1, 2 \tag{40}$$

$$S_1 = k^2 + \gamma_3^2 \tag{41}$$

and

$$L_1^2 = \frac{w_1 + \sqrt{w_1^2 - 4w_2}}{2} \tag{42}$$

$$L_2^2 = \frac{w_1 - \sqrt{w_1^2 - 4w_2}}{2} \tag{43}$$

$$S^2 = (\rho^*\chi_3 + 1)\delta^2 \tag{44}$$

$$w_1 = \frac{(m^*\delta^2 - \mathrm{i}b^*\delta)(\lambda^* + \alpha^2 M^* + 2) + M^*\delta^2 - 2\alpha M^*\rho^*\delta^2}{(\lambda^* + 2)M^*} \tag{45}$$

$$w_2 = \frac{(m^*\delta^2 - \mathrm{i}b^*\delta)\delta^2 - (\rho^*)^2\delta^4}{(\lambda^* + 2)M^*} \tag{46}$$

The radicals γ_i ($i = 1, 2, 3$) are selected such that $\mathrm{Re}(\gamma_i) \geqslant 0$. In above, L_1, L_2 and S are the non-dimensional wave number of three kinds of dispersive and dissipative body waves, i.e. two dilatational waves (fast and slow waves) and a rotational wave, respectively, propagating in a poroelastic solid.[2]

REFERENCES

1. M. A. Biot, 'General theory of three-dimensional consolidation', *J. Appl. Phys.*, **12,** 155–164 (1941).
2. M. A. Biot, 'Theory of propagation of elastic waves in a fluid-saturated porous solid: I. Low-frequency range; II. High-frequency range', *J. Acoust. Soc. Am.*, **28,** 168–191 (1956).
3. T. Senjuntichai and R. K. N. D. Rajapakse, 'Dynamic Green's functions of homogeneous poroelastic half-plane', *J. Engng. Mech. ASCE*, **120,** 2381–2404 (1994).
4. D. E. Beskos, 'Boundary element methods in dynamic analysis: part II (1986–1996)', *Appl. Mech. Rev.*, **50,** 149–197 (1997).
5. A. J. Philippacopoulos, 'Buried point source in a poroelastic half-space', *J. Engng. Mech. ASCE*, **123,** 860–869 (1997).
6. A. P. S. Selvadurai, *Elastic Analysis of Soil–Foundation Interaction*, Elsevier Scientific Publishing Co, Amsterdam, 1979.
7. M. R. Halpern and P. Christiano, 'Response of poroelastic half-space to steady-state harmonic surface tractions', *Int. J. Numer. Anal. Meth. Geomech.*, **10,** 609–632 (1986).
8. M. R. Halpern and P. Christiano, 'Steady-state harmonic response of a rigid plate baring on a liquid-saturated poroelastic half-space', *Earthquake Engng. Struct. Dyn.*, **14,** 439–454 (1986).
9. A. J. Philippacopoulos, 'Lamb's problem for fluid-saturated porous media', *Bull. Seism. Soc. Am.*, **78,** 908–923 (1988).
10. A. J. Philippacopoulos, 'Axisymmetric vibration of disk resting on saturated layered half-space', *J. Engng. Mech. ASCE*, **115,** 2301–2322 (1989).
11. M. K. Kassir and J. Xu, 'Interaction functions of a rigid strip bonded to saturated elastic half-space', *Int. J. Solid Struct.*, **24,** 915–936 (1988).
12. M. K. Kassir, K. K. Bandyopadhyay and J. Xu, 'Vertical vibration of a circular footing on a saturated half-space', *Int. J. Engng. Sci.*, **27,** 353–361 (1989).
13. S. Bougacha, J. L. Tassoulas and J. M. Roesset, 'Analysis of foundations on fluid-filled poroelastic stratum', *J. Engng. Mech. ASCE*, **119,** 1632–1648 (1993).
14. S. Bougacha, J. M. Roesset and J. L. Tassoulas, 'Dynamic stiffness of foundations on fluid-filled poroelastic stratum', *J. Engng. Mech. ASCE*, **119,** 1649–1662 (1993).
15. T. Senjuntichai and R. K. N. D. Rajapakse, 'Dynamics of a rigid strip bonded to a multilayered poroelastic half-plane', in A. P. S. Selvadurai (ed.), *Mechanics of Poroelastic Media*, Kluwer Dordrecht, Netherlands, 1996.
16. I. N. Sneddon, *Fourier Transforms*, McGraw-Hill, New York, 1951.
17. M. A. Biot, 'Mechanics of deformation and acoustic propagation in porous media', *J. Appl. Phys.*, **33,** 1482–1498 (1962).
18. P. Karasudhi, *Foundation of Solid Mechanics*, Kluwer Academic Publishers, Dordrecht, The Netherlands, 1990.
19. J. E. Luco and R. A. Westmann, 'Dynamic response of a rigid footing bonded to an elastic half-space', *J. Appl. Mech. ASME*, **39,** 527–534 (1972).
20. J. E. Luco and R. A. Westmann, 'Dynamic response of circular footings', *J. Engng. Mech. ASCE*, **95,** 1381–1394 (1971).
21. J. Lysmer and F. E. Jr. Richart, 'Dynamic response of footings to vertical loading', *J. Soil Mech. Found. Div. Proc. ASCE92* (SM1), 65–91 (1966).
22. R. K. N. D. Rajapakse and Y. Wang, 'Green's functions of transversely isotropic elastic half space', *J. Engng. Mech. ASCE*, **119,** 1724–1746 (1993).
23. R. Piessens, E. De Doncker-Kapenga, C. W. Uberhuber and D. K. Kahaner, *QUADPACK, A Subroutine Package for Automatic Integration*, Springer, Berlin, 1983.
24. R. Y. S Park and A. T. Gobert, 'Forced vertical vibrations of rigid disks with arbitrary embedment', *J. Engng. Mech. ASCE*, **117,** 2527–2548 (1991).

